# The B26 Cu-Zn-Ag-Au project, Brouillan volcanic complex, Abitibi greenstone belt, part 2: Hydrothermal alteration and mineralization

Quentin Fayard[1,2*], Patrick Mercier-Langevin[3], Réal Daigneault[1], Serge Perreault[2], and Natasha Wodicka[4]

[1]Université du Québec à Chicoutimi, 555 Boulevard de l'Université, Chicoutimi, Quebec G7H 2B1
[2]SOQUEM Inc., 1740 Chemin Sullivan, Val-d'Or, Quebec J9P 7H1
[3]Geological Survey of Canada, 490 rue de la Couronne, Québec, Quebec G1K 9A9
[4]Geological Survey of Canada, 601 Booth Street, Ottawa, Ontario K1A 0E8
[*]Corresponding author's e-mail: quentin.fayard@gmail.com

The B26 project is located in the northern Abitibi greenstone belt a few kilometres south of the past-producing Zn-Cu-Ag-Au Selbaie mine. It consists of a transposed Au-rich chalcopyrite stringer zone (Copper zone) overlain by concordant Ag-rich Zn-(Pb) sulphide lenses (Main Zinc zone) and disseminated to discordant sulphide vein- and veinlet-rich zones (Upper Zinc zone). The footwall rocks are affected by a wide and intense semi-conformable alteration halo mainly composed of sericite, chlorite, and quartz assemblages. Fe-Mn carbonate and quartz are common as gangue minerals in the sulphide lenses. The hanging-wall rocks are affected by a proximal K-feldspar-quartz and a more distal albite alteration with Fe-(Mn)-carbonate veins and replacement zones. The mineralized zones and host rocks have undergone major shortening during the main phase of regional deformation, which is responsible for transposition of the Cu-rich footwall stringers, flattening and stretching of the concordant semi-massive to massive sulphide zones, and local remobilization of precious metal-bearing phases into the south-dipping foliation and along the associated southwest-plunging stretching lineation.

Gold is directly associated with Cu, and also with Bi, Se, and Sn in the Copper zone as native gold, and Au-rich electrum with native Bi, bismuthinite, laitakarite, ikunolite, stannite, and cassiterite. Silver is present in the Main and Upper Zinc zones as freibergite, native silver, allargentum, acanthite, and pyrargyrite. Deposit-scale metal distribution and primary sulphide assemblages indicate that precious metals introduction was primary, although later local (metre-scale) remobilization occurred in response to deformation and metamorphism. Copper and Zn are decoupled at B26 and result from a strong vertical zonation in the system, suggesting an evolving geological environment with potentially a gradually shallowing seawater level. Shallow-water to subaerial conditions have been documented at the nearby Selbaie deposit, where they are considered responsible for the epithermal-style characteristics of the ore.

## INTRODUCTION

The B26 project is a recently discovered base and precious metals system hosted within the Brouillan volcanic complex in the northwestern Abitibi greenstone belt (Fig. 1). Total resources (indicated and inferred) are estimated at 11.4 Mt at 1.52% Cu, 1.19% Zn, 0.78 g/t Au, and 30 g/t Ag (Camus and Valdnais-LeBlanc, 2018). The Harricana-Turgeon belt, which comprises the Matagami and Joutel volcanogenic massive sulphide (VMS) camps (e.g. Legault et al., 2002; Debreil et al., 2018) and the Detour Lake orogenic gold deposit (e.g. Castonguay et al., 2020), have not been as extensively explored as other parts of the Abitibi belt, mostly due little surface exposure. The Brouillan volcanic complex has been studied because of its association with the Selbaie Zn-Cu-Ag-Au deposit that was mined between 1981 and 2004. The Selbaie deposit is distinctive amongst the polymetallic deposits of the Abitibi belt, as it has been interpreted as a possible Archean epithermal-like system formed in a shallow subaqueous to subaerial caldera environment (Deptuck et al., 1982; Larson, 1987; Faure et al., 1990, 1996; Larson and Hutchinson, 1993; Taner, 2000). Although some of the main features of the B26 mineralized zones are typical of precious metals-poor VMS deposits, they present some unusual characteristics. such as a strong decoupling of Cu and Zn, the association with calc-alkaline volcanic rocks, and anomalously high Ag contents (i.e. 100–2000 ppm Ag; Fayard et al., 2018). Selbaie and other mineralized zones of the Brouillan volcanic complex are also commonly characterized by high Ag grades and contents. This "provinciality"

Fayard, Q., Mercier-Langevin, P., Daigneault, R., Perreault, S., and Wodicka, N., 2020. The B26 Cu-Zn-Ag-Au project, Brouillan volcanic complex, Abitibi greenstone belt, part 2: Hydrothermal alteration and mineralization; *in* Targeted Geoscience Initiative 5: Contributions to the Understanding of Canadian Gold Systems, (ed.) P. Mercier-Langevin, C.J.M. Lawley, and S. Castonguay; Geological Survey of Canada, Open File 8712, p. 109–125. https://doi.org/10.4095/323669

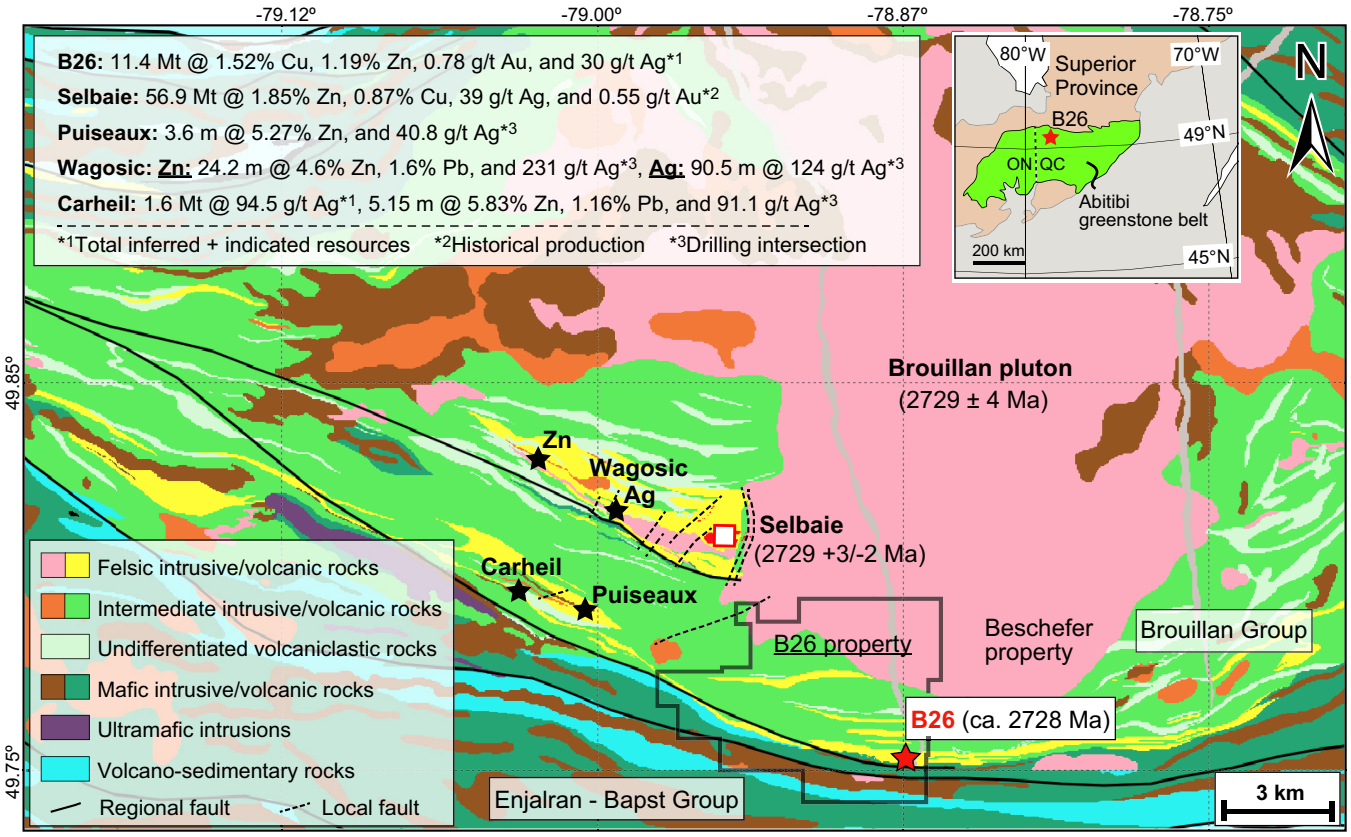


**Figure 1.** Geological map (*modified from* Faure, 2015) of the Brouillan volcanic complex showing the location of the B26 project and other significant deposits and prospects of the area. Ages are from Barrie and Krogh (1996) and Fayard et al. (2020).

regarding Ag and the presence of deposits with unusual styles of mineralization suggest that underlying factors may have controlled the precious metals budget (e.g. Mercier-Langevin et al., 2015).

This study is part of an ongoing M.Sc. project that aims at identifying the controls on the precious metal enrichment processes at B26. This report summarizes some of the main aspects of the metamorphosed and intensely deformed mineralized sulphide zones and hydrothermal alteration assemblages of the B26 project.

## Geological Setting

The geological setting of the B26 project is given in Fayard et al. (2020) and only the main features are summarized here. The B26 mineralized zones are hosted in a ca. 2729–2727 Ma (Barrie and Krogh, 1996; Fayard et al., 2020) homoclinal succession of steeply dipping, south-facing, intermediate to felsic volcanic rocks (Fig. 2a) that are part of the Brouillan Group of the Harricana-Turgeon belt in the northern part of the Abitibi greenstone belt. (Fig. 1). The Brouillan Group is underlain by the synvolcanic Brouillan pluton (Barrie and Krogh, 1996), which together form the Brouillan volcanic complex, and is overlain by the mafic-dominated Enjalran-Bapst Group to the south. The B26 project area is highly strained, as part of major east-west-trending deformation corridors located north and south of the Brouillan pluton (Lacroix, 1994; Daigneault et al., 2004), separating the volcanic packages and marking the contacts with the Taibi and Coapatina Archean metasedimentary rocks to the south and north, respectively. The main regional deformation ($D_p$), which is responsible for the east-west-trending foliation ($S_p$), is associated with greenschist-facies metamorphism that affects the area and mineralized zones of the B26 project.

The host succession to B26 comprises andesitic and dacitic units at the base (intermediate member) overlain by three distinct rhyolite units (Rhy A, Rhy B, and Rhy C: Fig. 2a). The rhyolite units are intercalated with andesite and sedimentary rocks in the uppermost part of the stratigraphic sequence. The rhyolite units, the uppermost sedimentary rocks, and andesite form the felsic member, which hosts most of the mineralized rocks and associated alteration (Adam, 1997; Beaudin, 2017; Fayard et al., 2020).

The felsic member hosts three mineralized zones that form the B26 deposit: 1) The Copper zone at the base (north); 2) the Main Zinc zone, separated into two mineralized bodies (eastern and western parts) along the same stratigraphic level, including the semi-massive to massive main lens as part of the easternmost body; and 3) the Upper Zinc zone located above the Main Zinc zone (Fig. 2a).

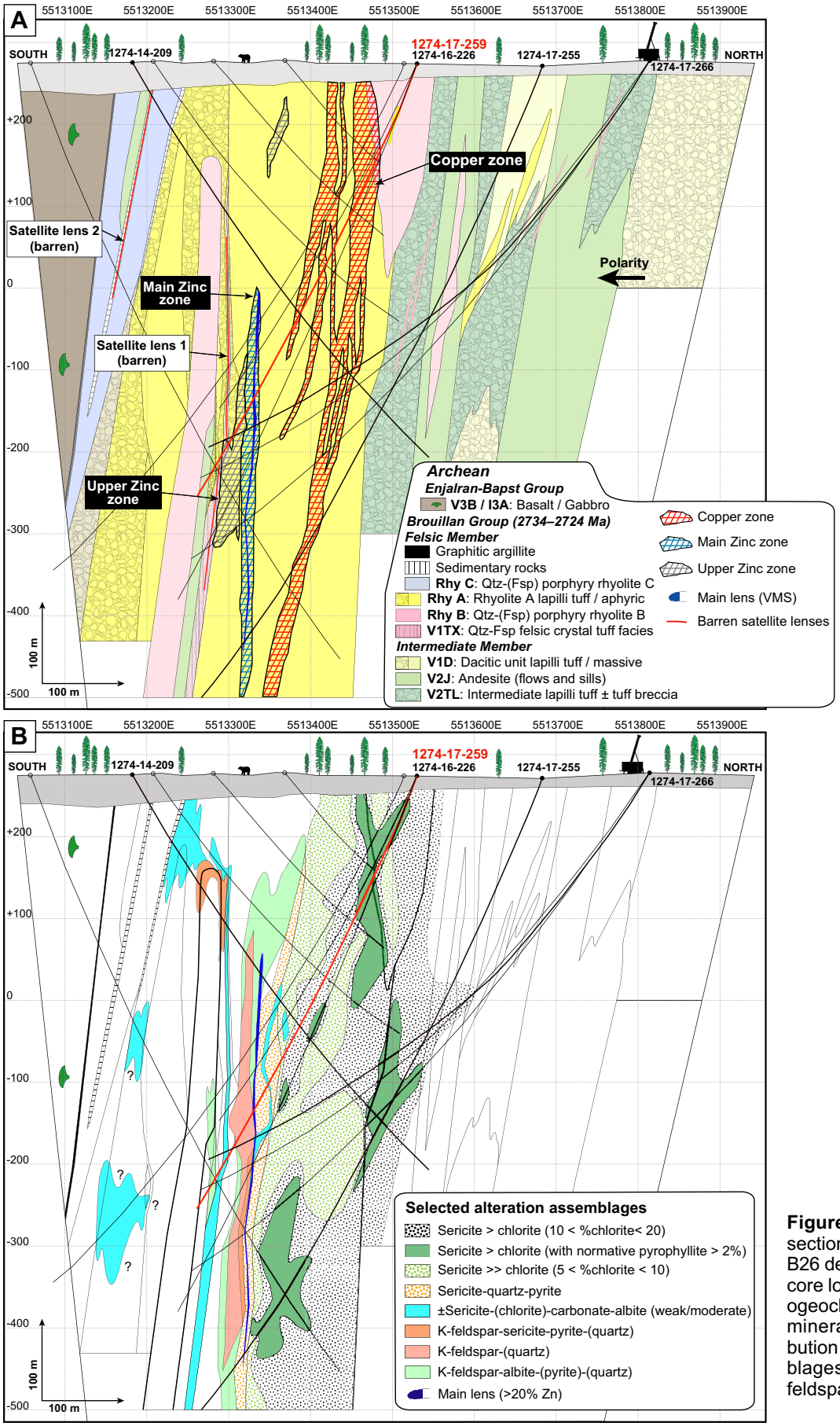


**Figure 2.** North-south cross-section (652950E ± 50 m) of the B26 deposit, established through core logging and whole-rock lithogeochemistry. **a)** Geology and mineralized zones. **b)** Distribution of the alteration assemblages. Abbreviations: Fsp = feldspar; Qtz = quartz.

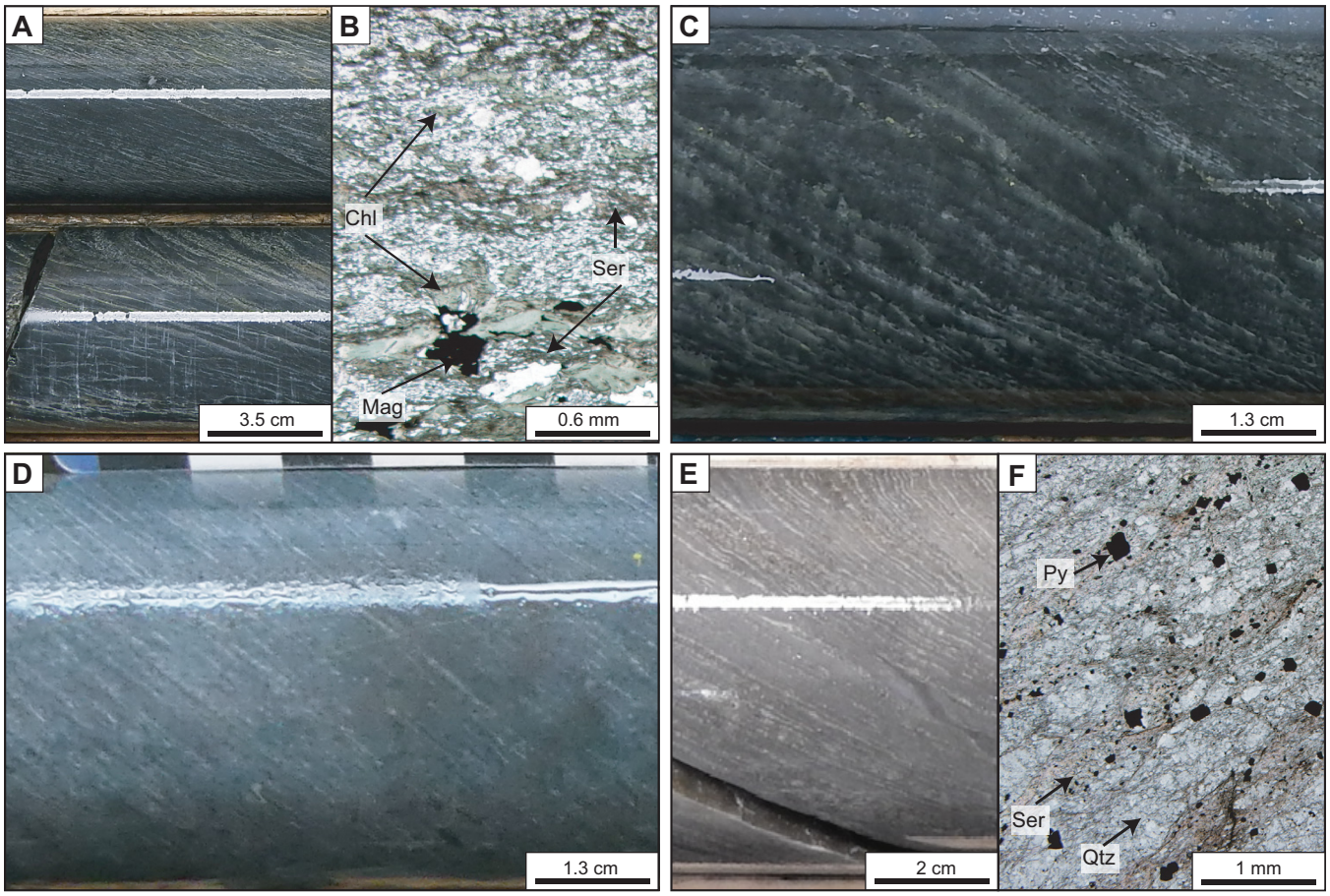


**Figure 3. a)** An example of the sericite ≥ chlorite alteration assemblage in rhyolite A. **b)** A photomicrograph (transmitted, natural light) of the sericite ≥ chlorite alteration assemblage. **c)** Chlorite > sericite alteration subassemblage. **d)** Sericite >> chlorite alteration subassemblage. **e)** An example of the sericite-quartz-pyrite alteration assemblage. **f)** A photomicrograph (transmitted, natural light) of the sericite-quartz-pyrite alteration assemblage. Abbreviations: Chl = chlorite, Mag = magnetite, Py = pyrite, Qtz = quartz, Ser = sericite.

## HYDROTHERMAL ALTERATION

Six alteration assemblages (containing 11 subassemblages, Table 1) are defined at B26 on the basis of mineralogy, mineral chemistry, whole-rock lithogeochemistry, and spatial distribution relative to the mineralized zone: 1) sericite-chlorite, 2) sericite-quartz-pyrite, 3) sericite-(chlorite)-albite-carbonate, 4) K-feldspar, 5) albite, and, 6) carbonate.

The paragenetic assemblages are metamorphosed and form alteration zones that are affected by regional deformation. Although the primary shape of the alteration zones has been variously transposed by the main schistosity, the primary geochemical compositions of each of the assemblages are largely preserved despite metamorphism. Readers are referred to Fayard (in prep) for details on the data, analytical procedures, methods, and for an in-depth description of the B26 alteration assemblages, geochemistry, and distribution and zonation.

The most abundant metamorphosed alteration minerals are sericite, chlorite, quartz, albite, carbonate, K-feldspar, pyrite, and locally biotite. Sericite (used here to define foliated, fine-grained aggregates of white mica; cf. Rieder et al., 1999) occurs as millimetre-thick bands that are parallel to the $S_p$ foliation and as fine (≤1 mm) porphyroblasts in the microcrystalline quartz±plagioclase matrix (Fig. 3e,f). Chlorite also occurs as millimetre thick bands that are parallel to the $S_p$ foliation and as isolated clusters or grains disseminated in the matrix (Fig. 3b). Chlorite and sericite are usually mixed in variable relative abundance, with sericite commonly replacing chlorite. Albite and K-feldspar (orthoclase) occur with quartz as micro-grains disseminated in the microcrystalline matrix, especially in the hanging-wall rhyolite A (Fayard, in prep). The carbonate alteration minerals are mainly represented by manganiferous siderite/ankerite/dolomite as gangue minerals in the Zn-rich sulphide zones (*see below*), and as pervasive and fracture-controlled alteration in the hanging-wall rocks. The predominant and widespread sericite-chlorite and sericite-quartz-pyrite alteration assemblages affect most of the B26 host rocks; detailed descriptions are provided below. The remaining four

**Table 1.** Alteration assemblages of the B26 deposit.

| Main assemblages | Subassemblages | Main minerals (vol.%) | Secondary minerals | Mass changes | Geometry |
|---|---|---|---|---|---|
| **Sericite-chlorite** | Chlorite > Sericite | 15 < Chlorite < 25%<br>5 < Sericite < 20%<br>(Rest = quartz) | pyrite, chalcopyrite | G: $Fe_2O_3^T$, MgO, $SiO_2$ | stratabound and discordant |
| | | | | L: $Na_2O$, $K_2O$, CaO, L-REE | |
| | Sericite ≥ chlorite | 15 < Sericite < 20%<br>10 < Chlorite < 20%<br>(Rest = quartz) | pyrite, chalcopyrite | G: $Fe_2O_3^T$, MgO | discordant |
| | | | | L: $Na_2O$, $K_2O$, CaO, $SiO_2$, L-REE | |
| | Sericite >> chlorite | 20 < Sericite < 30%<br>5 < Chlorite < 10%<br>(Rest = quartz) | pyrite, chalcopyrite, sphalerite | G: $Fe_2O_3^T$, MgO | stratabound and discordant |
| | | | | L: $Na_2O$, $K_2O$, CaO, $SiO_2$, L-REE | |
| **Sericite-quartz-pyrite** | | 20 < Sericite < 40%<br>2 < Pyrite < 5%<br>(Rest quartz) | chlorite, carbonate, biotite, sphalerite | G: $Fe_2O_{3T}$ | stratabound |
| | | | | L: $Na_2O$, $K_2O$, CaO, ($SiO_2$), L-REE | |
| **Sericite-(chlorite)-albite-carbonate** | | 5 < Sericite < 20%<br>2 < Chlorite < 5%<br>2 < Albite < 10%<br>(Rest = quartz) | carbonate, pyrite, K-feldspar | G: CaO, ($Fe_2O_3^T$, MgO) | stratabound and discordant |
| | | | | L: $Na_2O$, $K_2O$, $SiO_2$, | |
| **K-feldspar** | K-feldspar | K-feldspar > 30%<br>0 < Albite < 10%<br>(Rest = quartz) | pyrite, sphalerite, galena | G: $SiO_2$, $K_2O$ | stratabound |
| | | | | L: $Na_2O$, $Fe_2O_3^T$, MgO, CaO | |
| | K-feldspar-sericite-pyrite | K-feldspar > 20%<br>5 < Sericite < 20%<br>0 < Albite < 5%<br>2 < Pyrite < 3%<br>(Rest quartz) | pyrite, sphalerite | G: $SiO_2$, $K_2O$, $Fe_2O_3^T$ | stratabound |
| | | | | L: $Na_2O$, MgO, CaO | |
| | K-feldspar-Albite-Pyrite | 20 < K-feldspar < 30%<br>10 < Albite < 20%<br>1 < Pyrite < 3%<br>(Rest = quartz) | sphalerite, galena | G: $SiO_2$, $K_2O$, $Fe_2O_3^T$ | stratabound |
| | | | | L: $Na_2O$, MgO, CaO | |
| **Albite** | Albite dominated | 20 < Albite < 50% | K-feldspar, carbonate | | regional diffuse/pervasive |
| **Carbonates** | Carbonate-magnetite-(biotite)-pyrite veins and breccias | (Fe-Mg-Mn)-Carbonates (sideroplesite, pistomesite, ankerite, dolomite), Magnetite, Pyrite, (biotite) | sphalerite, pyrrhotite | G: $SiO_2$, $Fe_2O_3^T$, Cao, MgO, $Na_2O$ | discordant |
| | | | | L: $K_2O$ | |
| | Semi-massive to massive carbonates | (Fe-Mg-Mn)-Carbonates (sideroplesite, pistomesite, ankerite, dolomite), Magnetite | pyrite, pyrrhotite, stilpnomelane, chlorite | G: $Fe_2O_3^T$, $SiO_2$, CaO, MgO, $Na_2O$ | stratabound |
| | | | | L: $K_2O$ | |

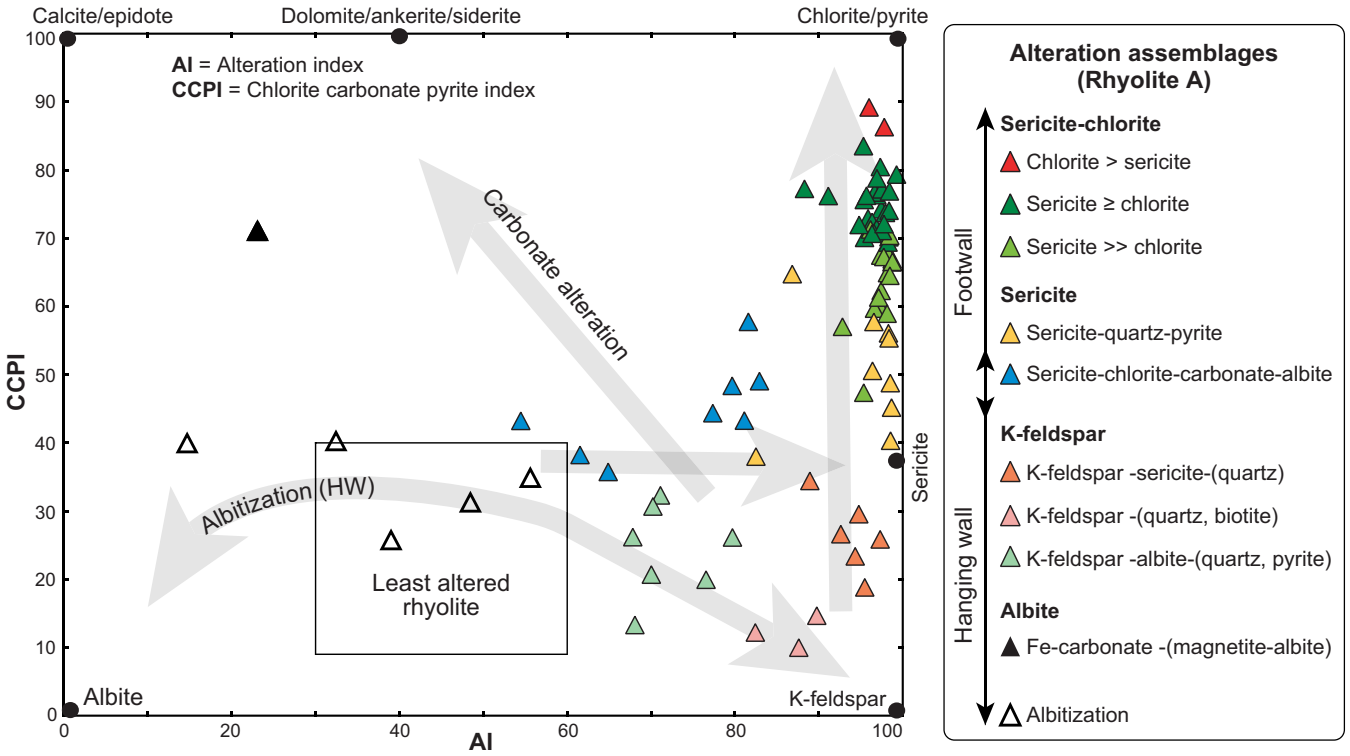


**Figure 4.** Alteration box plot of Large et al. (2001) of rhyolite A samples from the B26 project according to the alteration assemblages. AI = 100*[(MgO+$K_2O$)/(MgO+$K_2O$+$Na_2O$+CaO)] (Ishikawa et al., 1976), CCPI = 100*[(MgO+FeO)/(MgO+FeO+$K_2O$+$Na_2O$)] (Large et al., 2001).

assemblages are more localized; their principal characteristics are summarized in Table 1.

## Sericite-Chlorite Alteration Assemblage

The sericite-chlorite alteration assemblage dominates in the footwall of the Main Zinc zone and around the Copper zone (Fig. 2b). It is discordant to locally stratabound and affects most of the footwall sequence in the study area, reaching a total thickness of up to 200 m (Fig. 2b). Although this alteration assemblage is pervasive, fine-grained and generally $S_p$-foliated, primary volcanic textures are commonly preserved. The Hashimoto alteration index (AI: Ishikawa et al., 1976) and chlorite-carbonate-pyrite alteration index (CCPI: Large et al., 2001) values vary from moderate to strong (Fig. 4, 5). Light rare earth elements (LREE) are variably leached (Fayard, in prep). Mass balance calculations indicate significant gains in $Fe_2O_3^T$ and MgO, and variable losses in $Na_2O$, $K_2O$, and CaO (±$SiO_2$) (Fig. 5, Table 1; Fayard, in prep). Although it was not identified visually, the normative calculation (i.e. CONSONORM_LG, performed using Lithomodeleur software: Trépanier et al., 2015) indicates the presence of pyrophyllite locally in this assemblage (Fig. 2b). Mineral chemistry indicates that the sericite varies in composition from muscovite to phengite, with high $Al_2O_3$ (30–35 wt%), low FeO (<3 wt%), and very low to low MgO (0.8–3 wt%) content. Chlorite consists of ripidolite and is FeO-poor (25–32 wt%) and MgO-rich (10–15 wt%). Chlorite, in the selvages of chalcopyrite veins in the Copper zone, is Fe-rich (34–38 wt% FeO) and Mg-poor (6–8 wt% MgO). Sericite is the principal alteration-related mineral at B26 but, depending on the relative abundance of chlorite, the sericite-chlorite alteration assemblage can be subdivided into subassemblages.

### *Chlorite > sericite*

This subassemblage contains ≥20 vol.% chlorite and 5 to 20 vol.% sericite. It is present only locally, more commonly along chalcopyrite veins and locally at the contact with the main sulphide lens in the Main Zinc zone (e.g. diamond drillhole 1274-17-255: Fig. 2b). The zone comprising this subassemblage is discordant to stratigraphy, although transposed, except at the contact with the mineralized lens, where it is almost totally transposed. Chlorite dominates over sericite in this alteration facies (Fig. 3c), which represents some of the more geochemically altered rocks at B26 (Fig. 4). It is not mapped in Figure 2b as the sampling pattern was too widely spaced to allow a consistent representation in the section.

### *Sericite ≥ chlorite*

This subassemblage contains between 10 and 20 vol.% chlorite and 15 to 20 vol.% sericite (Fig. 3a,b). It is particularly well developed in the lowermost part of rhyolite A (Fig. 2b). It is spatially related to the Copper

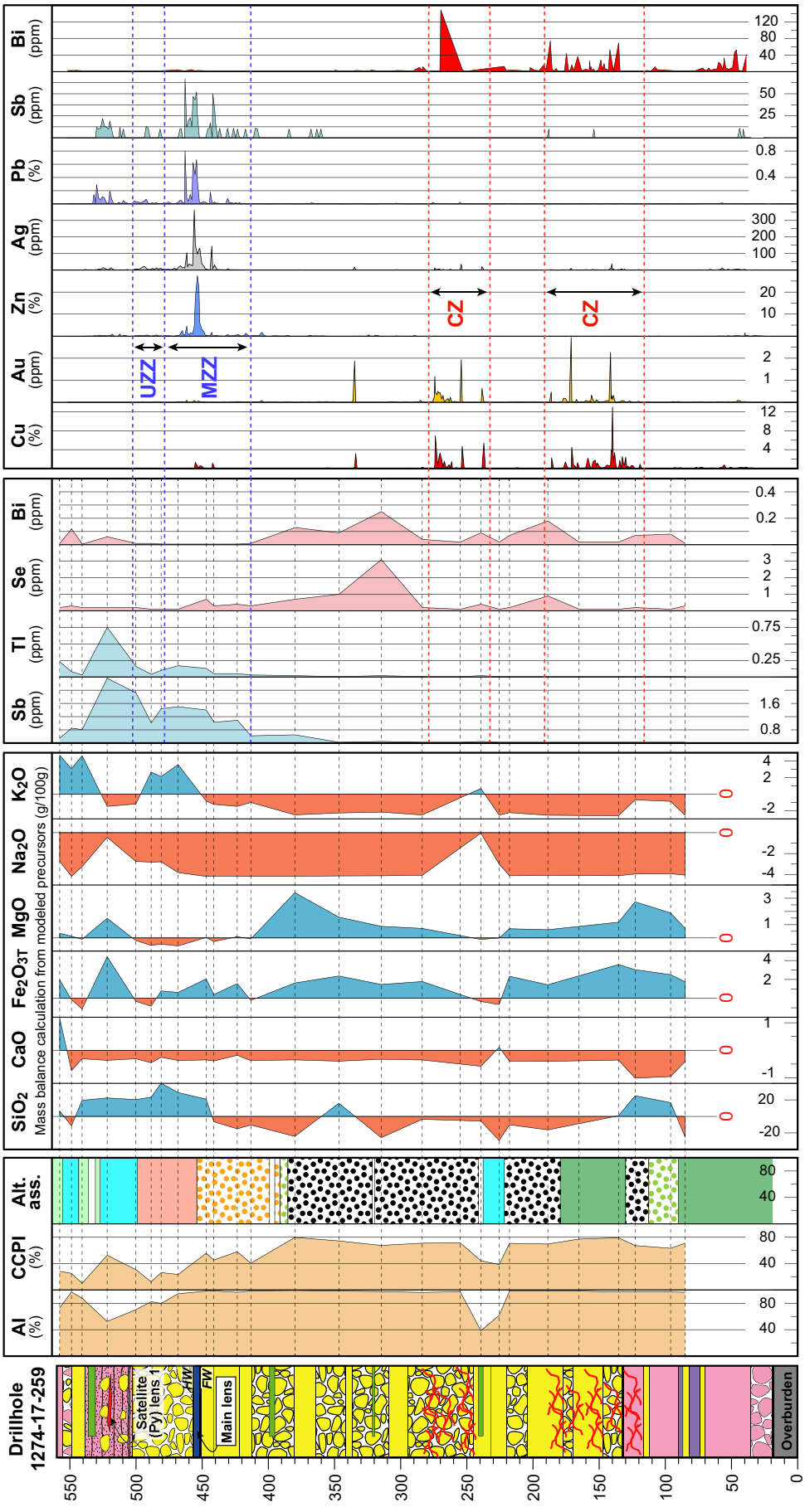


**Figure 5.** Simplified geology and geochemical profiles along drill core 1274-17-259 (see Fig. 2 for location, legend of lithological units, and formula for alteration indices). Alteration indices, mass balance calculations, and trace geochemistry are based on whole-rock geochemistry data and assays from SOQUEM. Mass balance calculations are based on the single precursor method of Trépanier et al. (2016). Abbreviations: AI = Hashimoto alteration index (Ishikawa et al., 1976), Alt. ass.= alteration assemblages, CCPI = chlorite-carbonate-pyrite alteration index (Large et al., 2001).

zone. Although strongly transposed, the geometry of this alteration seems to both be controlled by discordant structures and by the permeability of the volcaniclastic facies (Fig. 2b, Table 1). Rock units affected by this subassemblage alteration have high AI values and moderate CCPI values, in agreement with the dominant mineralogy (Fig. 4, 5).

### *Sericite >> chlorite*

This subassemblage contains between 5 and 10 vol.% chlorite and 20 to 30 vol.% sericite (Fig. 3d). It affects the footwall rhyolite A and B units (Fig. 2a) and corresponds to a "distal" halo to the Copper zone (Fig. 2b). It is more diffuse than the previous subassemblage, and its distribution and intensity are probably controlled predominantly by the primary permeability and porosity of the volcanoclastic facies. Rock units altered by this subassemblage have high AI values and low to moderate CCPI values, in agreement with dominant sericite over chlorite values (Fig. 4, 5).

## Sericite-Quartz-Pyrite Alteration Assemblage

This assemblage forms a stratiform band in the uppermost part of rhyolite A in the immediate footwall to the Main Zinc zone. It reaches its maximum thickness of about 30 m stratigraphically below the central part of the Main Zinc zone, and gradually decreases laterally (Fig. 2b). This concordant zone represents the proximal alteration assemblage underlying the massive main lens of the Main Zinc zone. It is composed of 20 to 40 vol.% sericite and 2 to 5 vol.% pyrite in a quartz± plagioclase groundmass (Fig. 3e,f). Pyrite abundance gradually increases towards the main lens. 1 to 2 vol.% of biotite porphyroblasts can be present a few metres under the main lens. Sericite occurs as closely spaced and strongly foliated millimetre thick bands (Fig. 3e,f).

The sericite-quartz-pyrite proximal footwall alteration assemblage has high alteration index values (AI >95: Fig. 4), with moderate CCPI values due to the absence of chlorite and generally low to moderate pyrite content. Rock units containing this assemblage show strong losses in $Na_2O$, limited $K_2O$ and CaO losses, and moderate $Fe_2O_3^T$ gains (pyrite) (Table 1). Light REE are also leached in the alteration assemblage, although not as strongly as in the sericite-chlorite assemblage (Fayard, in prep).

## Hanging-Wall Alteration Assemblages

Rock units in the hanging wall of the Main Zinc zone are weakly to locally moderately altered. Albite- and K-feldspar-bearing assemblages are usually of weak alteration intensity, except for the K-feldspar-sericite-pyrite subassemblage in which there can be up to 20 vol.% sericite. This latter subassemblage is proximal to the main lens, especially near its extremities, and generally transitional with the sericite-quartz-pyrite assemblage (Fig. 2b). The sericite (±chlorite)-carbonate-albite alteration assemblage occurs locally at the base of rhyolite B within the crystal tuff facies (Main Zinc zone hanging wall) and as discordant zones in the volcaniclastic facies of the uppermost part of rhyolite A (Fig. 2b). Although common at B26, carbonate alteration has not been systematically mapped since its footprint is diffuse. Carbonates (Fe-Mg-Mn-Ca) are present in veins, as matrix fill in rhyolite breccias, and as pervasive zones in the rhyolite C. The hanging-wall rock units are characterized by variable and heterogeneously distributed mass gains in $SiO_2$, $Fe_2O_3^T$ (due to Fe-carbonates) and locally in $K_2O$ (Fig. 5, Table 1).

# MINERALIZED ZONES

Several sulphidized intervals have been intersected by drilling on the B26 property (Adam, 1997; Beaudin, 2017). The Copper zone, the Main Zinc zone, and the Upper Zinc zone represent the most significant and continuous mineralized zones (Fig. 2a, 5, 6). Two thin, relatively continuous, but barren pyrite-(pyrrhotite) satellite lenses are located higher in the stratigraphic sequence. The latter are not discussed in this report; *see* Fayard (in prep) for details.

## Copper Zone

The Copper zone is the largest mineralized zone at B26, both in total tonnage and extent. It consists of several juxtaposed mineralized intervals (Fig. 5, 6) that are discontinuous and transposed/flattened into the $S_p$ foliation. It is located in the footwall of the Main Zinc zone, near the base of the felsic member, within rhyolite A and in the upper part of the lowermost rhyolite B unit (Fig. 2a). It can be up to 60 m thick and extends down to at least 1100 m below surface. It is interpreted to represent a strongly flattened or transposed feeder zone below the concordant Zn-rich zones (Fayard et al., 2018).

The Copper zone comprises stringer-style and disseminated Cu-bearing sulphide zones (Fig. 7a). The stringers locally form centimetre- to decimetre-thick semi-massive to massive sulphide veins (Fig. 7b) that contain variable amounts of quartz and carbonates. Durchbewegung structures (cf. Marshall and Gilligan, 1989) are common in the massive sulphide veins (Fig. 7b). Chalcopyrite is the main mineral and accounts for more than 95 vol.% of the sulphides. Pyrite generally constitutes 2 vol.% of the ore but can locally reach up to 20 vol.%. Pyrrhotite and sphalerite can be present in minor amounts, except very locally where they can reach up to 10 vol.%. Native gold is common in the chalcopyrite-rich stringers. Also, Bi-, Se-, and locally Sn-bearing trace minerals are present in chalcopyrite, as shown by whole-rock analyses (Table 2).

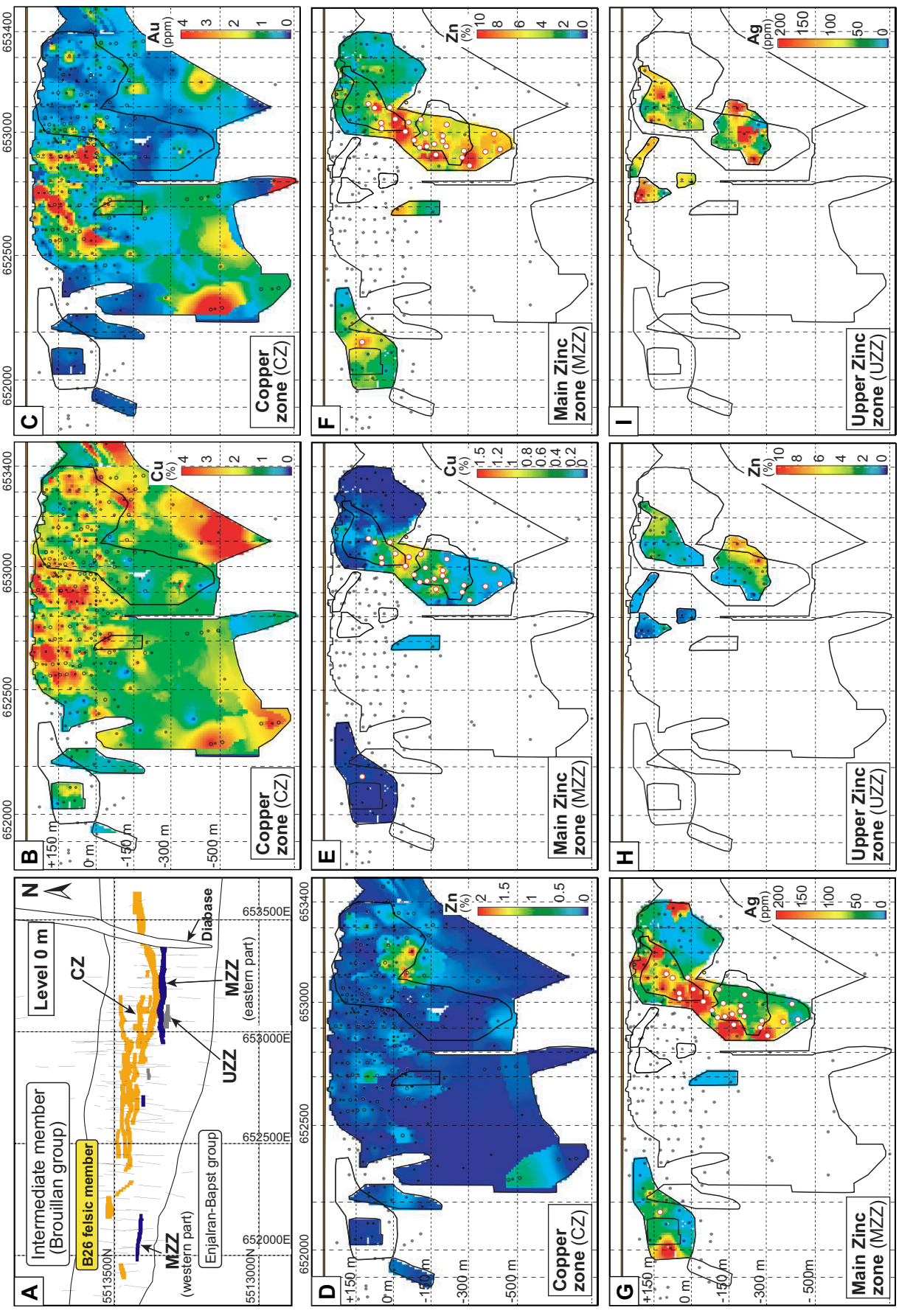


**Figure 6**. Interpolation (method given in Camus and Valdnais-Leblanc, 2018) of the Cu-Zn-Au-Ag values, showing the distribution of metals for each mineralized zone in an average longitudinal section: **a)** level 0 m plan view (± 50 m) of the mineralized zones; **b)** copper in CZ; **c)** gold in CZ; **d)** zinc in CZ; **e)** copper in MZZ; **f)** zinc in MZZ; **g)** silver in MZZ; **h)** zinc in UZZ; and **i)** silver in UZZ. Composite data are from Camus and Valdnais-Leblanc (2018). White circles with red contours represent semi-massive to massive sulphides in the MZZ. Abbreviations: CZ = Copper zone, MZZ = Main Zinc zone, UZZ = Upper Zinc zone.

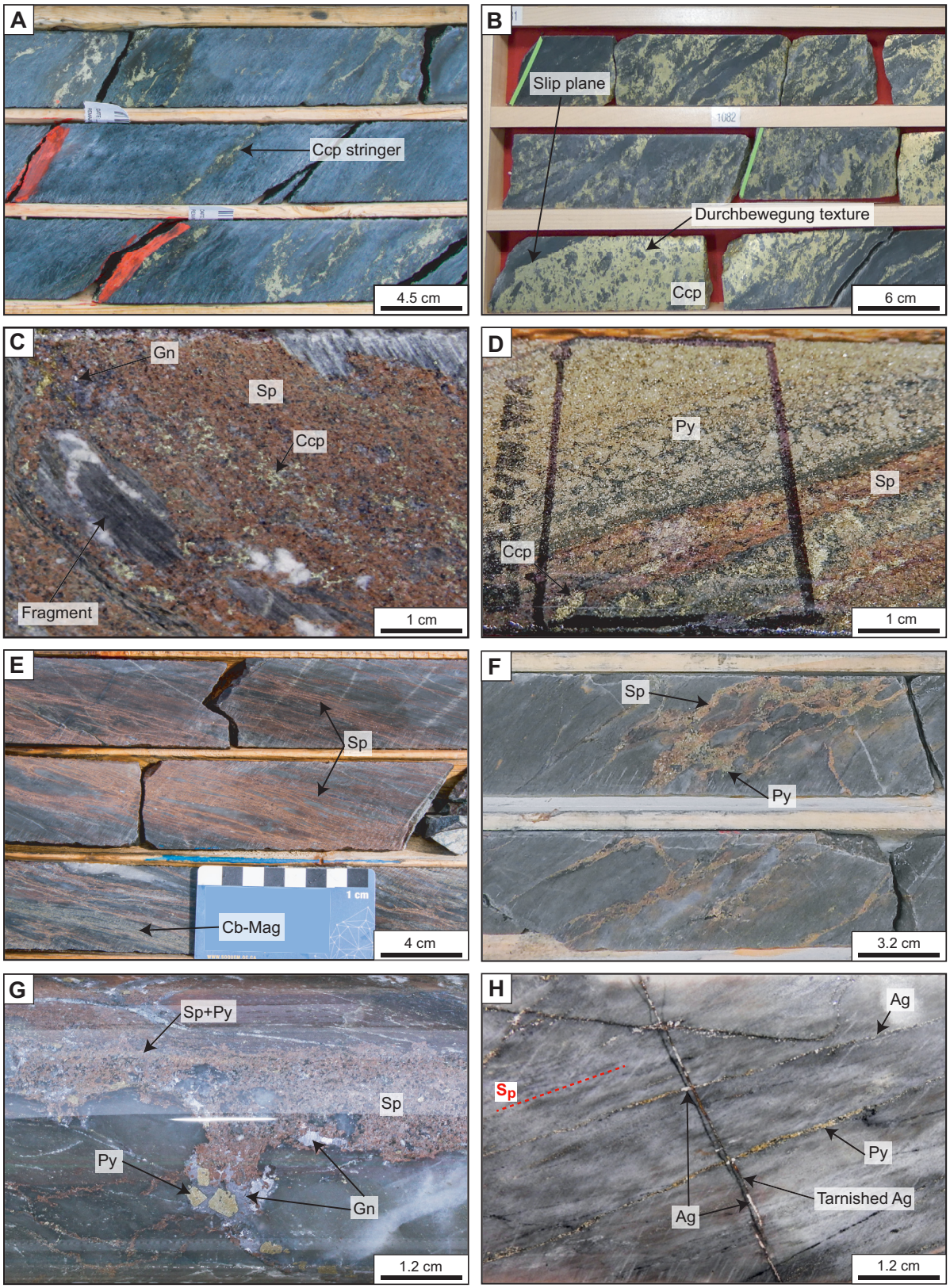


**Figure 7. a and b)** Semi-massive to massive chalcopyrite veins/stringers of the Copper zone, with sliding planes and durchbewegung texture. **c)** Massive sphalerite-rich ore of the Main Zinc zone (MZZ), with rounded rhyolite fragments. **d)** Massive pyrite-rich ore of the MZZ, with tectonometamorphic banding with sphalerite. **e)** Sphalerite-rich stratabound replacement mineralization of the Upper Zinc zone (UZZ) hosted in volcaniclastic rhyolite A. **f)** Sphalerite-pyrite veinlets/stringers hosted in MZZ hanging-wall rhyolite A. **g)** Polymetallic silver-rich piercement vein composed of sphalerite and galena with pyrite porphyroblasts. **h)** Native silver microveinlets of the UZZ that crosscut the main foliation ($S_p$). Abbreviations: Ag = silver, Cb = carbonate mineral, Ccp = chalcopyrite, Gn = galena, Mag = magnetite, Py = pyrite, Sp = sphalerite.

**Table 2.** Whole-rock geochemistry for selected elements of representative ore samples.

| Zone | Copper Zone | | Main Zinc Zone | | | | | |
|---|---|---|---|---|---|---|---|---|
| Type | SMS veins/stringers | | MS | | | SMS | | DS |
| *Sample #* | ***23_144.1*** | ***245_860.6*** | ***266_666.7*** | ***259_451.9*** | ***250_294.4*** | ***259_454.5*** | ***238_605.7*** | ***259_455.9*** |
| **Cu** (%) | 14.35 | 12.6 | 0.28 | 0.74 | 0.22 | 1.04 | 0.36 | 2.12 |
| **Zn** (%) | 0.105 | 0.04 | 24.4 | >30 | 16.85 | 12.4 | 7.44 | 1.605 |
| **Pb** (ppm) | 35.8 | 13.7 | 5440 | 650 | 13600 | 4610 | 1760 | 397 |
| **Au** (ppm) | 4.55 | 19.95 | 0.057 | 0.061 | 0.059 | 0.058 | 0.016 | 0.081 |
| **Ag** (ppm) | 37.8 | 23.1 | 191 | 149 | 419 | 171 | 122 | 388 |
| **Au/Ag** | 1 : 8.3 | 1 : 1.2 | 1 : 3350 | 1 : 2442 | 1 : 7101 | 1 : 2948 | 1 : 7625 | 1 : 4790 |
| **$SiO_2$** (%) | 39 | 49 | 13.4 | 12.45 | 15.2 | 44.5 | 20.1 | 32.4 |
| **CaO** (%) | 0.31 | 0.02 | 0.98 | 0.77 | 5.22 | 0.51 | 3.56 | 5.86 |
| **Fe** (%) | 19.45 | 13.8 | 22.9 | 20.1 | 18.4 | 13.95 | 28.5 | 23.4 |
| **Mn** (%) | 0.37 | 0.03 | 0.19 | 0.15 | 0.17 | 0.3 | 0.46 | 0.96 |
| **S** (%) | 17 | 13.6 | 35 | 32.6 | 26.8 | 14.2 | 27.2 | 4.3 |
| **As** (ppm) | 12.7 | 3.3 | 178.5 | 195.5 | 1450 | 153.5 | 1190 | 633 |
| **Bi** (ppm) | 1205 | 602 | 20.9 | 1.67 | 0.93 | 1.55 | 2.05 | 0.21 |
| **Cd** (ppm) | 3.34 | 0.84 | >1000 | >1000 | >1000 | 698 | 470 | 114 |
| **Sb** (ppm) | 4.5 | 2.04 | 47.6 | 12.2 | 333 | 33.6 | 15.25 | 12.35 |
| **Se** (ppm) | 143 | 114 | 44 | 29 | 5 | 2 | 12 | 1 |
| **Sn** (ppm) | 112 | 173 | 3.2 | 7.1 | 17.3 | 5.4 | 8 | 1.3 |
| **Tl** (ppm) | 0.05 | 0.25 | 0.54 | 1.21 | 1.92 | 4.12 | 1.24 | 3.18 |
| **Sum REE** | 26.48 | 74.78 | 15.47 | 22.14 | 237.15 | 26.38 | 12.16 | 37.72 |

## Main and Upper Zinc Zones

The Main Zinc zone consists of two mineralized bodies that are divided into a western and eastern part and are located at the same stratigraphic level. The largest one is situated in the eastern part of the deposit (Fig. 2a, 6) and forms a subvertical panel that plunges 65° to the southwest with a thickness ranging from 40 m close to surface, to roughly 10 m at about 750 m below surface. It has a lateral extent of approximately 400 m. The easternmost mineralized body hosts the only occurrence of semi-massive to massive mineralization (white/red circles on Fig. 6e,f,g), named the main lens, which has the same geometry.

The Upper Zinc zone is less continuous and consists of small mineralized panels that are hosted in rhyolite A, in the hanging wall of the Main Zinc zone. The lateral extension can be up to 200 m long and the thickness varies from 3 to 25 m (Fig. 2a). The best intervals contain up to 10 wt% Zn.

The Main and Upper Zinc zones show four mineralization styles: 1) semi-massive to massive sulphides; 2) disseminated sulphides; 3) sulphide veins and stringers; and 4) silver-rich veins and veinlets. Whole-rock analyses of representative samples for each mineralization style are given in Table 2.

### *Semi-massive to massive sulphides*

The semi-massive to massive Zn-bearing sulphide lens (i.e. main lens), which is up to 3.5 m thick, is more massive at the base (north) with ≥65 vol.% sulphides and becomes semi-massive (35–65 vol.% sulphides) towards the top of the lens. Sphalerite is the most abundant phase (20–60 vol.%: Fig. 7c), although pyrite can locally dominate (20–40 vol.%: Fig. 7d). Pyrite is generally recrystallized (granoblastic), although porous and/or nodular primary textures are locally partly preserved (Fayard, in prep). Chalcopyrite (1–5 vol.%) is mainly found at the base in the central part of the lens. Galena (≤2 vol.%) is present in association with sphalerite in the uppermost part of the lens. Native Ag and Ag-sulphosalts (e.g. freibergite) are common in the massive sulphides in the presence of galena. Magnetite is also present (1–3 vol.%) in the upper semi-massive part of the Main Zinc zone. Carbonate minerals are common as gangue in the massive sulphide zones. The sulphide assemblages are generally deformed and are largely recrystallized. Wall-rock fragments of host rhyolite A are common in the massive and semi-massive sulphides (Fig. 7c).

### *Disseminated sulphides*

Zones of disseminated sulphides are present on both sides of the semi-massive to massive sulphides of the Main Zinc zone. Disseminated sulphides are also associated with the Upper Zinc zone. These zones mainly comprise finely disseminated pyrite and sphalerite. Total sulphide abundance generally varies between 2 to locally 10 vol.%, with pyrite more abundant than sphalerite.

The central part of the Upper Zinc zone is composed of 10-40 vol.% reddish sphalerite in very thin (0.2–1 mm) veinlets or stringers, and bands (Fig. 7e) that transition into a carbonate-pyrite-(magnetite) assemblage at the top of the zone. Laterally, this mineralization is more deformed and remobilized, forming semi-massive breccia zones with quartz and rhyolite clasts in a sphalerite matrix.

### *Sulphide veins and stringers*

Zones of sulphide veins and stringers, strongly flattened into the $S_p$ foliation, are common in the hanging wall to the Main and Upper Zinc zones in rhyolite A (Fig. 2a). Some of the veins appear to be late- to post-deformation as they cut across the $S_p$ foliation.

A zone of sulphide veins and stringers is located within 5 m under (north) the main massive sulphide lens of the Main Zinc zone. These 0.2 to 5 cm thick veins and veinlets are partly to completely transposed into the $S_p$ foliation. The veins consist of sphalerite ±pyrite-chalcopyrite.

A second zone of veinlets and veins is located in the upper part of the Main Zinc zone. This hanging-wall veining is better developed where the Main Zinc zone is devoid of massive sulphides (e.g. westernmost part, and easternmost part, close to surface: Fig. 6). These 0.2 to 2 cm thick veins mainly consist of reddish to orange sphalerite with pyrite and, very locally, galena. The veins appear as both tabular, parallel with the $S_p$ foliation, and as a relatively weakly deformed anastomosing network in fragmental intervals (Fig. 7f). These sphalerite-rich vein and stringer zones are locally enriched in Ag in the presence of galena.

### *Silver-rich veins and veinlets*

This type of mineralization consists of polymetallic piercement veins and Ag microveinlets. Piercement veins are common in the uppermost part of the massive sulphide lens in the Main Zinc zone, as well as in the Upper Zinc zone. Such veins are considered late as they cut across the $S_p$ foliation and are not associated with a specific alteration. They are up to a few centimetres thick and contain variable amounts of sulphides and quartz. Sulphides typically consist of sphalerite and galena, with lesser amounts of other sulphides (Fig. 7g). Chalcopyrite is locally present, as well as some granoblastic pyrite. Piercement sulphide veins generally contain high Ag (typically 70–500 ppm) and Sb grades (≤300 ppm). The Ag-bearing accessory phases are mainly freibergite, allargentum, and less commonly, pyrargyrite and stephanite.

The Ag microveinlets are parallel and/or at a high sharp angle to the $S_p$ foliation, forming a network pattern (Fig. 7h). They carry the highest Ag grades (commonly >1000 ppm) of the deposit. These veins are rectilinear, undeformed, and cut across the foliation, and are thus considered as late features that represent remobilized material in post-$S_p$ fractures. Such Ag-rich microveinlets are common in the Upper Zinc zone where they contain abundant native silver with some micro-grains of automorphic pyrite. They are also locally present in the Main Zinc zone (under the main lens), where they contain acanthite instead of native Ag close to Fe-poor sphalerite veinlets.

## Metal Distribution

Assay data from SOQUEM were used to illustrate the longitudinal metal distribution in the Copper, Main, and Upper Zinc zones, as shown in Figure 6. Interpolation methods, based on Camus and Valdnais-Leblanc (2018), are described in Fayard (in prep).

Copper distribution is represented on a composite longitudinal view because Cu-rich intervals are present at different stratigraphic positions in the footwall rhyolite A, where it occurs as several juxtaposed flattened bodies (Fig. 2a, 6a). Copper is unevenly distributed in the Copper zone. It is mainly concentrated close to surface and in several separate areas at depth (Fig. 6b), whereas Zn concentrations are very low except where the Copper zone converges with the Main Zinc zone (Fig. 6a,d). An area of lower Cu values in the Copper zone underlies the Main Zinc zone. Copper grades are low and much localized in the Main Zinc zone (Fig. 6e). The Main Zinc zone occurs as two separate mineralized bodies at the same stratigraphic horizon (Fig. 6a,f). Slightly higher in the stratigraphy is the Upper Zinc zone (Fig. 6a,h). Zinc in the Main Zinc zone occurs in a steeply southwest-plunging ore shoot that is parallel with the stretching lineation, which also parallels Cu distribution in the Copper zone. Gold is concentrated in the Copper zone and the distribution and geometry of the higher grade zones mimic those of Cu, although less laterally extensive (Fig. 6c). The high-grade zones are also parallel with the $L_p$ stretching lineation, forming narrow shoots.

Silver grades are very low in the Copper zone (typically ≤20 ppm, 6.7 ppm on average). However, it is strongly enriched in the Main Zinc zone (average 100.4 ppm), where its distribution mimics that of Zn (Fig. 6g). Higher Ag grades (>200 ppm) occur mainly along the western edge of the massive sulphide lens of the Main Zinc zone. In the Upper Zinc zone, Ag is present in all the mineralized zones (average 138 ppm) with common intersections at 200 to >1000 ppm. These very high Ag values do not necessarily correlate with higher Zn grades (Fig. 6h,i). Moreover, although not illustrated in the longitudinal views shown in Figure 6, Pb is commonly associated with some of these high-Ag values (Fig. 5) but not the highest, which is a reflection of the complex mineralogy of Ag.

Despite significant syn-$D_p$ transposition, flattening, and stretching in the direction of the $L_p$ lineation, the deposit-scale metal distribution is still typical of many Archean VMS deposits with an Au-bearing stringer-style Cu-rich zone at the base and a stratiform Ag-bearing zinc lens in the upper part (Hannington, 2014). The Cu-rich part of the main lens at 653000 mE in the Main Zinc zone (Fig. 6e) probably represents the main upflow zone and corresponds to the area where the slightly discordant (transposed) Copper zone draws close to the Main Zinc zone at depth (Fig. 2a, 6a).

### *Precious metal-bearing phases*

Gold occurs as ≤200 µm native gold grains in chalcopyrite, associated locally with sphalerite and pyrrhotite (Fig. 8a,b) or in quartz (Fig. 8c). Gold has a Ag content of 20 wt% on average with some electrum (i.e. Ag content >45 wt%) in the Main Zinc zone. Micron-size Bi- and Se-bearing sulphides are common in the Copper zone: bismuthinite ($Bi_2S_3$), laitakarite ($Bi_4Se_2S$), ikunolite ($Bi_4(S,Se)_3$), and native Bi have been identified (Fig. 8d,e). Traces amounts of stannite ($Cu_2FeSnS_4$) and cassiterite ($SnO_2$) are also present in the chalcopyrite of the Copper zone.

Silver-rich minerals and Ag-Sb sulphosalts are common in the Main and Upper Zinc zones. Freibergite ($(Cu,Ag)_{10}(Fe,Zn)_2Sb_4S_{13}$), which is generally associated with galena (Fig. 8f), is the main Ag-bearing mineral. It is also common in veinlets intergrown with anhedral native silver and allargentum ($Ag_{1-x}Sb_x$), chalcopyrite, and galena (Fig. 8g). Pyrargyrite ($Ag_3SbS_3$) and stephanite ($Ag_5SbS_4$) are locally present in freibergite masses and in galena-rich veins, where pyrargyrite replaces pyrrhotite, forming complex secondary textures associated with allargentum. Native silver is common and mainly appears in the late crosscutting microveinlets and disseminations in the Upper Zinc zone and in small complex clusters (associated with chalcopyrite-freibergite intergrowths) in galena.

## DISCUSSION

### Primary and Secondary Controls on Mineralization Styles and Geometry

Although the volcanic pile that hosts the B26 deposit has been tilted and strongly deformed (flattening, stretching, and transposition), primary features are partly preserved. The overall geometry of the mineralized system, comprising chalcopyrite stringers associated with a subconcordant to slightly discordant sericite-chlorite halo that lies underneath concordant Zn-rich sulphide lenses, is typical of many Archean and younger VMS deposits (Galley et al., 2007).

Although intensely transposed, the Cu-rich veins and proximal chlorite-sericite alteration assemblage of the Copper zone are still slightly discordant to the stratigraphic sequence and $S_p$ foliation. The veins are both rooted in the rhyolite B and in the footwall andesites and are connected with the stratiform sulphide lens of the Main Zinc zone in the uppermost part of rhyolite A. Therefore, the Copper zone is interpreted as an extensive discordant stringer zone that has been flattened and transposed during the main ($D_p$) deformation event.

The Main Zinc zone overlies the Copper zone sulphide stringers and forms a stratabound to stratiform ore lens (main lens) hosted in rhyolite A in a large, semi-concordant sericite-dominated alteration halo. The Main Zinc zone probably formed between two separate flows of rhyolite A (Fayard et al., 2020). The presence of massive sulphides along a specific horizon suggests that part of the Main Zinc zone may have formed through exhalative activity on the seafloor. However, a large part of the mineralization was formed by subseafloor replacement, as indicated by the presence of partly preserved volcaniclastic rocks in the semi-massive, disseminated, and vein-style mineralization in both the footwall and hanging wall as well as in the massive sulphide intervals and by the stacking of mineralized zones in the stratigraphic sequence. Thus, it is suggested that the hanging-wall rhyolite A was emplaced soon after the beginning of the massive sulphide lens deposition at, or near the seafloor, making the calc-alkaline rhyolite A emplacement and hydrothermal activity broadly coeval at about 2728 Ma, the age of rhyolite A (Fayard et al., 2020). The thin (0.5–1.5 m thick) satellite semi-massive pyrite lens located above the Upper Zinc zone (in the rhyolite B felsic crystal tuff facies) and associated with moderate sericite-carbonate-albite alteration (Fig. 2a, 4) seems to be the product of late low-temperature and metal-poor fluids. These fluids were locally trapped due to an impermeable barrier formed by sills of rhyolite B in the volcanoclastic facies of rhyolite A, perhaps marking the waning stages of the B26 hydrothermal system.

### Metal Zonation and Conditions of Deposition

Contrary to many Archean VMS deposits that show a gradual transition from Cu-rich basal to Zn-rich top parts (e.g. Noranda deposits: Galley et al., 2007), Cu and Zn are strongly decoupled at the deposit-scale at B26. The Copper, Main, and Upper Zinc zones are located at different stratigraphic levels and the mineralized system extends over a large part of the volcanic pile, i.e., ≥200 m after tectonic flattening. The original thickness of the host package and the vertical extent of the mineralized system can only be speculated, but using a conservative flattening ratio of 5-to-1 given by the volcanic clasts aspect ratio, the system might have had an original vertical extent of well over 500 m. As

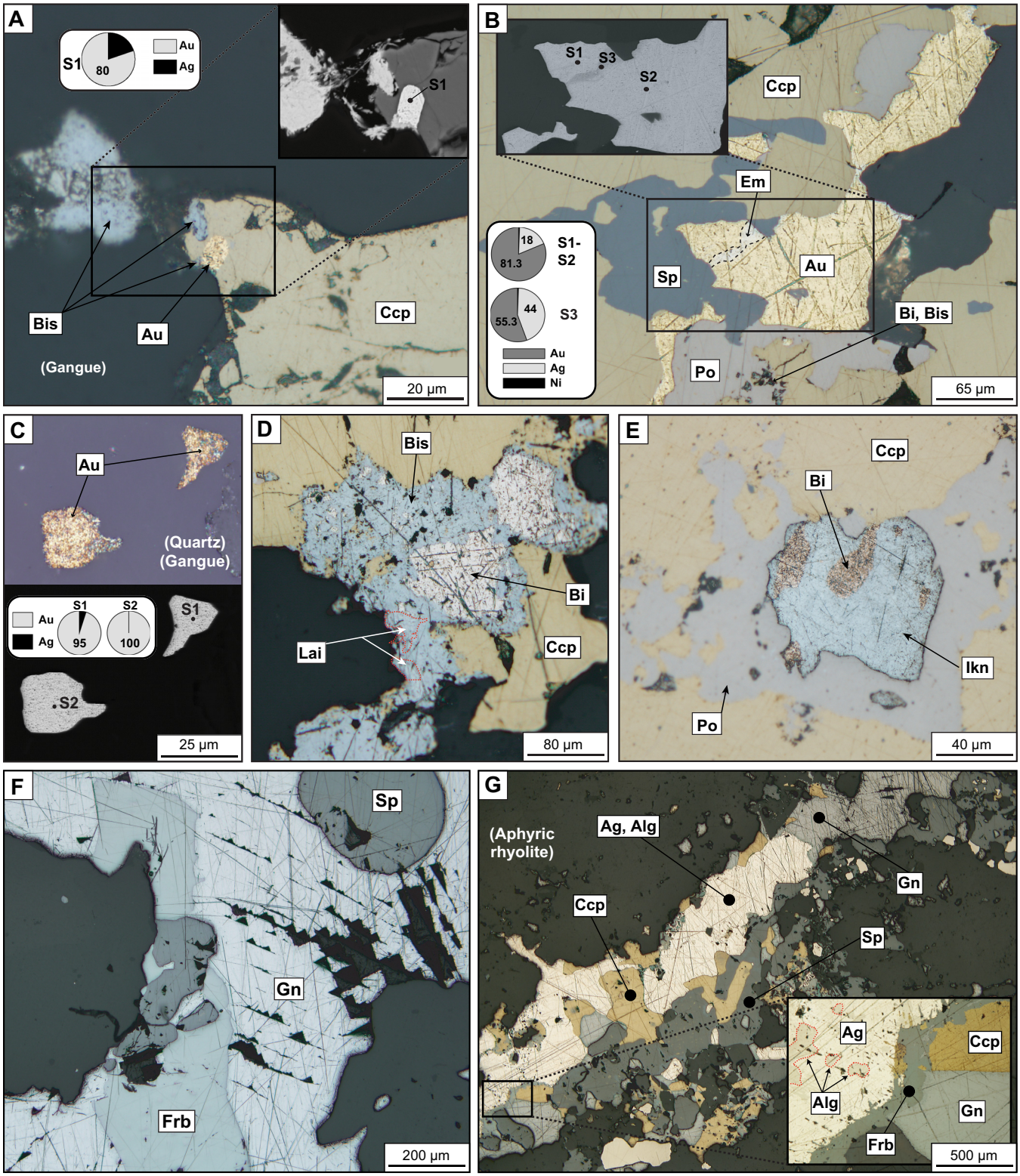


**Figure 8.** Reflected light microphotographs of ore assemblages. **a)** Gold-rich electrum and bismuthinite in chalcopyrite in the Copper zone. **b)** Native gold intergrown with minor Au-rich electrum and micrograins of native bismuth and bismuthinite in chalcopyrite, sphalerite, and pyrrhotite in the Copper zone. **c)** Free gold grains in the matrix of a chalcopyrite vein of the Copper zone. **d)** Bismuthinite, laitakarite, and native Bi in chalcopyrite, Copper zone. **e)** Native bismuth and ikunolite in pyrrhotite, Copper zone. **f)** Freibergite in galena in a piercement vein, Upper Zinc zone. **g)** Veinlet composed of complex intergrowths of native silver and allargentum, associated with freibergite, chalcopyrite, sphalerite, and galena within a polymetallic piercement vein, Upper Zinc zone. Abbreviations: Alg = allargentum, Au = gold, Bi = bismuth, Bis = bismuthinite, Em = electrum, Frb = freibergite, Ikn = ikunolite, Lai = laitakarite, Po = pyrrhotite, $S_1$ to $S_3$ = spot EDS semi-quantitative analyses.

in a classic VMS model, Cu at B26 was probably transported as a chloro-complex in high-temperature (325–375ºC), slightly acidic fluids, with conductive cooling over a significant vertical gradient as the main precipitating factor (Hannington, 2014). Zinc, Pb, and Ag were transported much higher up in the system as thio-complexes in lower temperature fluids that were destabilized through mixing with seawater (Galley et al., 2007). Such a geometry with such a strong decoupling of metals (Cu vs Zn-Pb) is tentatively interpreted as originating from a shallow water system in which metal transport and precipitation are largely controlled by the seawater boiling curve (e.g. Hannington, 2014).

Gold is mostly associated with Cu and the high-temperature assemblage (Bi, Se, Sn±In) at B26. Such an association is compatible with the transport of Au by chloro-complexes ($AuCl_2$) along with Cu (Huston, 2000).

Silver can precipitate at both high and low temperatures, depending on the redox state, pH, and Sb-Bi content of the fluid, and thus Ag can be incorporated in a wide range of host minerals (Huston et al., 1996). At B26, freibergite is the principal Ag-bearing mineral in the inferred low-temperature assemblage of the Main and Upper Zinc zones. According to Huston et al. (1996), this indicates that Ag has precipitated at low temperature from relatively oxidized fluids characterized by low ΣAs/ΣSb and ΣBi/ΣSb ratios. No micro-analyses of galena from B26 are available, but given the very low ΣBi/ΣSb ratio of bulk samples, galena is probably Sb-rich, in which case it can incorporate less Ag, and thus favours the precipitation of Ag-Sb sulphosalts. However, Huston et al. (1996) mention that there are exceptions to their model (e.g. Heath-Steele and Rosebery deposits) where Ag-Sb sulphosalts are stabilized under reduced conditions from low-temperature fluids. More work is underway to better constrain the possible nature of the Ag-transporting fluids at the B26 deposit.

Finally, the potassic feldspar-quartz microcrystalline alteration assemblage characterizing a part of the hanging-wall rhyolite A (Fig. 2b) could indicate low temperatures and near-neutral pH fluids buffered by mixing with ambient seawater at the margin of the hydrothermal system (e.g. Thalanga deposit: Paulick et al., 2001).

## Source of Precious Metals and Possible Primary Enrichment Mechanisms

Silver and Pb are known to have been initially present in greater amounts in continental crust-derived rhyolites (Barrie and Hannington, 1999). However, Archean VMS deposits of the Abitibi greenstone belt are generally considered associated with oceanic-crust-derived rocks that have, in most cases, low Pb and Ag (Barrie and Hannington, 1999). Archean calc-alkaline felsic centres have empirically been associated with some of the largest synvolcanic Au deposits of the southern Superior Province (e.g. Doyon-Bousquet-LaRonde camp: Mercier-Langevin et al., 2015; Yergeau et al., 2015, Horne 5: Krushnisky et al., 2020, and Rainy River: Pelletier et al., 2015), suggesting an association between magmatic processes and precious metal-bearing volcanogenic hydrothermal systems in the southern Superior Province (e.g. Mercier-Langevin et al., 2015). Although more work is needed to determine the precise nature of the mineralizing fluid(s) and source(s) of metals at B26, some elements suggest the potential involvement of magmatic volatiles in the hydrothermal system (Fig. 9). This includes the presence of trace elements such as Bi, Se, Sn, and In (Table 2), a strong Au and Bi correlation (r = 0.75: Fayard, in prep), and the spatial and temporal association with the Brouillan synvolcanic pluton and the Selbaie epithermal-style (Larson and Hutchinson, 1993) Zn-Cu-Ag-Au deposit.

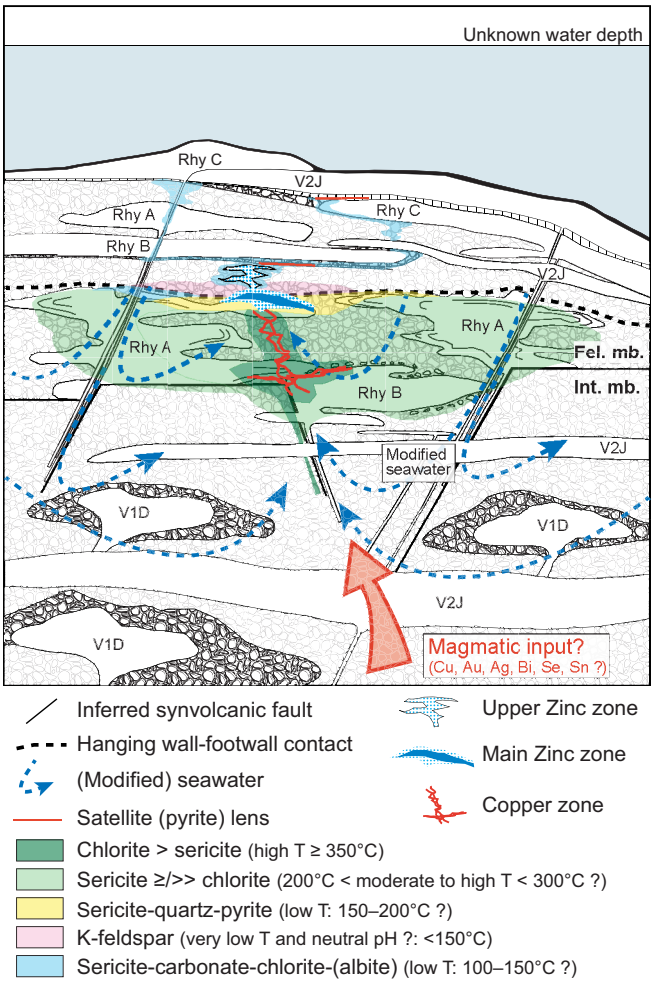


**Figure 9.** Inferred pre-deformation hydrothermal architecture of the B26 deposit. Lithological unit colours have been removed but codes and textural patterns are the same as in Figure 2a. Abbreviations: Fel. mb. = felsic member, Int. mb. = intermediate member, mod. = moderate, T = temperature.

### Effect of Metamorphism and Deformation on Precious Metals Distribution

The general spatial correlation between Au and Cu distribution in the Copper zone and its association with other trace metals such as Bi are in agreement with a syngenetic introduction of Au in the system. However, the occurrence of higher grade Au zones as narrow shoots parallel to the stretching lineation suggests local (metre scale or less) remobilization during the main deformation.

Silver in the Main and Upper Zinc zones was locally remobilized due to metamorphism and deformation, but its overall association with the syngenetic sulphide zones also indicates a primary synvolcanic origin. Evidence of mechanical remobilization is given by the presence of post-$S_p$ piercement veins with pyrite and sphalerite transitioning to chalcopyrite, galena, and sulphosalts in the tip of the veins due to the increasing ductility of these phases. Further remobilization, probably through chemical processes (solubilization), led to the crystallization of native Ag in very late fractures and the gradual increase in the Ag grade of piercement veins and fractures. Chemical remobilization is also supported by the presence of galena and sulphosalts at pyrite grain boundaries. The presence and solubility of Sb largely control Ag grades and distribution (remobilization) adjacent to the sulphide zones. Freibergite is the main Ag-bearing phase within and in proximity to the sulphide lenses. Therefore, the Sb:Ag ratio controls the nature of the Ag-bearing phases with a transition from freibergite (proximal to trace metal-bearing sulphide source) to allargentum to native Ag away from the sulphide zones.

Silver-rich mineralization is not unique to B26 and seems to be a recurring feature in the Brouillan volcanic complex area. The Selbaie deposit is known for very high-grade Ag intersections, commonly as native silver and freibergite (Larson and Hutchinson, 1993; Taner, 2000). Numerous prospects hosted in the Brouillan volcanic complex (e.g. Wagosic, Carheil, and Puiseaux: SIGÉOM, 2019 - Fig. 1) also contain significant Ag in both VMS-style and vein-style ore systems. This suggests the presence of some underlying, district-scale controls on the precious metal enrichment processes, which are the subject of ongoing research as part of this study.

## ACKNOWLEDGMENTS

This report is a contribution to the Targeted Geoscience Initiative Program of the Geological Survey of Canada. Support for this study was provided through the Gold Project Activity G- 1.1: Gold through space and time at the Archean. Q. Fayard is conducting a TGI-supported M.Sc. at the Université du Québec à Chicoutimi. The authors would like to thank SOQUEM Inc. for their support and collaboration in this study and access to data. This report benefited from constructive comments by D. Yergeau and S. Castonguay.

## REFERENCES

Adam, D., 1997. Rapport d'une campagne de forage, propriété B26, canton Brouillan, Québec, Canada; Les métaux Billiton Canada Inc., GM 57187, 14 p.

Barrie, C.T. and Hannington, M.D., 1999. Classification of volcanic-associated massive sulfide deposits based on host-rock composition; in Volcanic-associated massive sulfide deposits: Processes and examples in modern and ancient settings, (ed.) C.T. Barrie and M.D. Hannnington; Reviews in Economic Geology, v. 8, p. 1–11.

Barrie, C.T. and Krogh, T.E., 1996. U-Pb zircon geochronology of the Selbaie Cu-Zn-Ag-Au mine, Abitibi Subprovince, Canada; Economic Geology, v. 91, p. 563–575.

Beaudin, A., 2017. Rapport de la campagne de sondages hiver-été 2014, propriété B26, canton Brouillan, Québec, Canada; SOQUEM Inc., GM 70058, 45 p.

Camus, Y. and Valdnais-Leblanc, O., 2018. Rapport Technique NI 43-101 et estimation des ressources, Projet B26, Québec; Unpublished internal report to SOQUEM Inc., 136 p.

Castonguay, S., Dubé, B., Wodicka, N., and Mercier-Langevin, P., 2020. Geological setting and gold mineralization associated with the Sunday Lake and Lower Detour deformation zones, northwestern Abitibi greenstone belt, Ontario and Quebec; *in* Targeted Geoscience Initiative 5: Contribution to the Understanding of Canadian Gold Systems, (ed.) P. Mercier-Langevin, C.J.M. Lawley, and S. Castonguay; Geological Survey of Canada, Open File 8712, p. 127–1142. doi:10.4095/323670

Daigneault, R., Mueller, W.U., and Chown, E.H., 2004. Abitibi greenstone belt plate tectonics: the diachronous history of arc development, accretion and collision; in The Precambrian Earth: Tempos and events, (ed.) P.G. Eriksson, W. Altermann, D.R. Nelson, W.U. Mueller, and O. Catuneanu; Developments in Precambrian Geology 12, p. 88–103.

Debreil, J.-A., Ross, P.-S., and Mercier-Langevin, P., 2018. The Matagami district, Abitibi greenstone belt, Canada: Volcanic controls on Archean volcanogenic massive sulfide deposits associated with voluminous felsic volcanism; Economic Geology, v. 113, p. 891–910.

Deptuck, R., Squair, H., and Wierzbicki, V., 1982. Geology of the Detour zinc–copper deposits, Brouillan Township, Quebec; *in* Precambrian sulfide deposits, H.S. Robinson Memorial Volume, (ed.) R.W. Hutchinson, C.D. Spece, and J.M. Franklin; Geological Association of Canada, Special Paper 25, p. 319–342.

Faure, S., 2015. Prolongement de la faille Sunday Lake (mine Detour Gold, Ont.) au Québec et son potentiel pour les minéralisations aurifères et en métaux de base; CONSOREM Project 2013-02, 41 p. < http://www.consorem.ca/production_scientifique/2013_02/Rapport%202013-02%20DETOUR_VF_20160401.pdf> [accessed November 15, 2019]

Faure, S., Jébrak, M., and Bouillon, J.J., 1990. Géologie et minéralisations en Zn–Cu–Ag–Au de Les Mines Selbaie; *in* The northwestern Quebec polymetallic belt; A summary of 60 years of mining exploration; Proceedings of the Rouyn-Noranda 1990 symposium, (ed.) M. Rive, P. Verpaelst, Y. Gagnon, J.M. Lulin, G. Riverin, and A. Simard; Canadian Institute of Mining and Metallurgy, Special Volume 43, p. 363–372.

Faure, S., Jébrak, M., and Angelier, J., 1996. Structural evolution of Les Mines Selbaie, northern Abitibi, Québec, Canada; Exploration and Mining Geology, v. 5, p. 215–230.

Fayard, Q., Mercier-Langevin, P., Daigneault, R., and Perreault, S., 2018. Volcanic, hydrothermal and structural controls on the nature and distribution of base and precious metals at the B26 project, Brouillan volcanic complex, Abitibi, Quebec; *in* Targeted Geoscience Initiative: 2017 report of activities, volume 1, (ed.) N. Rogers; Geological Survey of Canada, Open File 8358, p. 99–103.

Fayard, Q., Mercier-Langevin, P., Wodicka, N., Daigneault, R., and Perreault, S., 2020. The B26 Cu-Zn-Ag-Au project, Brouillan volcanic complex, Abitibi, part 1: Geological setting and geochronology; *in* Targeted Geoscience Initiative 5: Contribution to the Understanding of Canadian Gold Systems, (ed.) P. Mercier-Langevin, C.J.M. Lawley, and S. Castonguay; Geological Survey of Canada, Open File 8712, p. 93–107. doi:10.4095/323668

Galley, A.G., Hannington, M.D., and Jonasson, I.R., 2007. Volcanogenic massive sulphide deposits; *in* Mineral deposits of Canada: A synthesis of major deposit-types, districts metallogeny, the evolution of geological provinces, and exploration methods, (ed.) W.D. Goodfellow; Geological Association of Canada, Mineral Deposits Division, Special Publication 5, p. 141–161.

Hannington, M.D., 2014. Volcanogenic massive sulfide deposits; *in* Treatise on Geochemistry (Second Edition), Volume 13: Geochemistry of Mineral Deposits, (ed.) S. Scott; Elsevier Science, Netherlands, p. 463–488.

Huston, D.L., 2000. Gold in volcanic-hosted massive sulphide deposits; distribution, genesis, and exploration; *in* Gold in 2000, (ed.) S.G. Hagemann and P.E. Brown; Reviews in Economic Geology, v. 13, p. 401–426.

Huston, D.L., Jablonski, W., and Sie, S.-H., 1996. The distribution and mineral hosts of silver in eastern Australian volcanogenic massive sulfide deposits; The Canadian Mineralogist, v. 34, p. 529–546.

Ishikawa, Y., Sawaguchi, T., Iwaya, S., and Horiuchi, M., 1976. Delineation of prospective targets for Kuroko deposits based on modes of volcanism of underlying dacites and alteration haloes; Mining Geology, v. 26, p. 105−117.

Krushnisky, A., Mercier-Langevin, P., Ross, P.-S., Goutier, J., Pilote, C., and Bernier, C., 2020. Geology and gold enrichment at the Horne 5 Archean volcanogenic massive sulphide deposit, Abitibi greenstone belt, Quebec: a synthesis; *in* Targeted Geoscience Initiative 5: Contribution to the Understanding of Canadian Gold Systems, (ed.) P. Mercier-Langevin, C.J.M. Lawley, and S. Castonguay; Geological Survey of Canada, Open File 8712, p. 31–44. doi:10.4095/323663

Lacroix, S., 1994. Géologie de la partie ouest du sillon Harricana-Turgeon, Abitibi; Ministère des Ressources naturelles du Québec, MB 94-54, 26 p.

Large, R.R., Gemmell, J.B., Paulick, H., and Huston, D.L., 2001. The alteration box plot: A simple approach to understanding the relationship between alteration mineralogy and lithogeochemistry associated with volcanic-hosted massive sulfide deposits; Economic geology, v. 96, p. 957–971.

Larson, J.E., 1987. Geology, geochemistry and volcanic history of Les Mines Selbaie, Quebec, Canada: An Archean epithermal system; Ph.D. thesis, Colorado School Mines, Golden, Colorado, 388 p.

Larson, J. E. and Hutchinson, R. W., 1993. The Selbaie Zn-Cu-Ag deposits, Quebec, Canada; an example of evolution from subaqueous to subaerial volcanism and mineralization in an Archean caldera environment; Economic Geology, v. 88, p. 1460−1482.

Legault, M., Gauthier, M., Jébrak, M., Davis, D., and Baillargeau, F., 2002. Evolution of the subaqueous to near-emergent Joutel volcanic complex, Northern Volcanic Zone, Abitibi Subprovince, Quebec, Canada; Precambrian Research, v. 115, p. 187−221.

Marshall, B. and Gilligan, L.B., 1989. Durchbewegung structure, piercement cusps, and piercement veins in massive sulfide deposits: formation and interpretation; Economic Geology, v. 84, p. 2311–2319.

Mercier-Langevin, P., Hannington, M.D., Dubé, B., Piercey, S.J., Peter, J.M., and Pehrsson, S.J., 2015. Precious metal enrichment processes in volcanogenic massive sulphide deposits – a summary of key features, with an emphasis on TGI-4 research contributions; *in* Targeted Geoscience Initiative 4: Contributions to the understanding of volcanogenic massive sulphide deposits genesis and exploration methods development, (ed.) J.M. Peter and P. Mercier-Langevin; Geological Survey of Canada Open File 7853, p. 117–130.

Paulick, H., Herrmann, W., and Gemmell, B., 2001. Alteration of felsic volcanics hosting the Thalanga massive sulfide deposit (Northern Queensland, Australia) and geochemical proximity indicators to ore; Economic Geology, v. 96, p. 1175–1200.

Pelletier, M., Mercier-Langevin, P., Dubé, B., Crick, D., Tolman, J., McNicoll, V.J., Jackson, S.E., and Beakhouse, G.P., 2015. The Rainy River "atypical" Archean Au deposit, western Wabigoon Subprovince, Ontario; *in* Targeted Geoscience Initiative 4: Contributions to the understanding of Precambrian lode gold deposits and implications for exploration, (ed.) B. Dubé and P. Mercier-Langevin; Geological Survey of Canada, Open File 7852, p. 193–207.

Rieder, M., Cavazzini, G., D'yakonov, Y.S., Frank-Kemenetskii, V.A., Gottardi, G., Guggenheim, S., Koval, P.V., Müller, G., Neiva, A.M.R., Radoslovich, E.W., Robert, J.-L., Sassi, F.P., Takeda, H., Weiss, Z., and Wones, D.R., 1999. Nomenclature of the micas; Mineralogical Magazine, v. 63, p. 267−279.

SIGÉOM, 2019. Système d'information géominière du Québec. Ministère de l'Énergie et des Ressources Naturelles. <http://sigeom.mines.gouv.qc.ca> [accessed November 15, 2019]

Taner, M. F., 2000; The Geology of the volcanic-associated polymetallic (Zn, Cu, Ag and Au) Selbaie deposits, Abitibi, Quebec, Canada; Exploration and Mining Geology, v. 9. p. 189−214.

Trépanier, S., Mathieu, L., and Daigneault, R., 2015. CONSONORM_LG: New normative minerals and alteration indexes for low-grade metamorphic rocks; Economic Geology, v. 110, p. 2127–2138.

Trépanier, S., Mathieu, L., Daigneault, R., and Faure, S., 2016. Precursors predicted by artificial neural networks for mass balance calculations: Quantifying hydrothermal alteration in volcanic rocks; Computers & Geosciences, v. 89, p. 32–43.

Yergeau, D., Mercier-Langevin, P., Dubé, B., Malo, M., McNicoll, V.J., Jackson, S.E., Savoie, A., and La Rochelle, F., 2015. The Archean Westwood Au deposit, southern Abitibi: Telescoped Au-rich VMS and intrusion-related Au systems; *in* Targeted Geoscience Initiative 4: Contributions to the understanding of Precambrian lode gold deposits and implications for exploration, (ed.) B. Dubé and P. Mercier-Langevin; Geological Survey of Canada, Open File 7852, p. 177−191.